J Mater Sci (2009) 44:1560–1571
DOI 10.1007/s10853-008-3163-3

SYNTACTIC AND COMPOSITE FOAMS

Whispering gallery mode-based micro-optical sensors for structural health monitoring of composite materials

Nguyen Quang Nguyen · Nikhil Gupta ·
Tindaro Ioppolo · M. Volkan Ötügen

Received: 15 November 2007 / Accepted: 5 December 2008 / Published online: 15 January 2009

Abstract Development of smart materials with inherent damage sensing capabilities is of great interest to aerospace and other structural applications. Most of the existing smart materials are based on using embedded sensors for structural health monitoring. However, embedded sensors can lead to undesirable effects such as stress concentration and can cause premature failure. Therefore, using microstructural components for additional function of sensing of the structural health is the only option. Such possibilities exist only in selected few materials. The present study investigates the feasibility of developing fiber- and particle-reinforced composites into smart materials. The sensing approach considered is based on the morphology-dependent shifts of optical modes, referred to as the whispering gallery modes (WGMs), of spherical dielectric micro-particles. The WGMs are excited by coupling light from a tunable diode laser using single mode fibers. The WGMs of the micro-particles can be observed as sharp dips in the transmission spectrum through the fiber and are highly sensitive to the morphology of the particle. A minute change in the size, shape, or refractive index causes a shift of the optical modes, which can be interpreted quantitatively in terms of the parameter that caused the change. A theoretical framework is developed for such sensor systems that provides quantitative relations between the stress applied on the micro-particles and corresponding shift in WGMs. These relations are validated against the available experimental results.

Introduction

High-performance fiber- and particle-reinforced composite materials are widely used in aerospace, automobile, and marine structures. In all applications, early detection of damage is desirable to enhance the safety and reliability of the structure or the system. In addition, the detection of damage is carried out by a variety of sensors, which can either continuously monitor the structural health and the ambient conditions or are triggered by any of the parameters that cross the threshold. Sensors of small size and light weight are usually preferred because of the possible adverse effects of large sensors on the structural integrity. Various types of sensors commonly used in materials include piezoelectric particles, acoustic emission sensors, and optical fibers. Each type of sensors has its benefits and limitations. Several studies can be found in the published literature elaborating on the sensing schemes and capabilities of smart materials containing these sensors.

Use of fiber-optic sensors is advantageous in composite materials because they can become an integral part of the structure and provide strengthening in addition to the sensing function. Examples of fiber-optic sensors include fiber Bragg grating (FBG) sensors [1–3], intrinsic or extrinsic Fabry–Pérot sensors (IFPI or EFPI) [4, 5], high-birefringence polarimetric sensors [6, 7], and white-light interferometric sensors [8]. Use of these sensors in

N. Q. Nguyen · N. Gupta (✉)
Composite Materials and Mechanics Laboratory, Mechanical and Aerospace Engineering Department, Polytechnic Institute of New York University, Brooklyn 11201, USA
e-mail: ngupta@poly.edu

N. Q. Nguyen
e-mail: nnguye02@students.poly.edu

T. Ioppolo · M. V. Ötügen
Micro-Sensors Laboratory, Mechanical Engineering Department, Southern Methodist University, Dallas, TX 75275, USA

composite plates and filament wound pipes has been studied, where one of the glass fibers is replaced by an optical fiber for sensing [9]. These sensing schemes are successful in detecting stress, strain, or temperature inside the structure. However, the FBG sensors have low sensitivity compared to other similar sensors. In particular, the optical quality factor, Q, which is one of the main parameters in determining the upper limit of measurement resolution, is typically limited to 1,000 for FBG and 3,000 for EFPI sensors. In comparison, the Q-factor for whispering gallery mode (WGM)-based sensors can be over 10^6. Additionally, each sensor type has some disadvantages. The EFPI sensors do not provide a direct value of the quantity that is measured and need a demodulation, which may be expensive [10]. Birefringence polarimetric sensor's sensitivity is significantly affected by several factors including fluctuations in the input light source, fiber bending, and detector noise [11]**.** The sensors based on white-light interferometry can help in avoiding some of the problems associated with the conventional interference techniques such as in FBG and IFPI/EFPI. However, applications of these techniques require substantial experience for interpretation of results, and they are not sensitive enough to detect small changes in the quantity that is measured [12]. Moreover, the sensitivity of such sensors is not high enough to provide information on the crack initiation and small changes in the detection parameters.

In the present study, the concept of WGM sensors is investigated for health-monitoring applications in composite materials. In WGM sensors, a dielectric microparticle (typically, a sphere with diameter of the order of ~100 μm) is side coupled to an optical fiber. One end of the fiber is coupled to a tunable laser while a photodetector is coupled to the other end, which monitors the transmission spectrum through the fiber-particle system. As the laser is tuned, the optical modes (resonant frequencies) of the micro-particle appear as sharp dips in the transmission spectrum. These optical modes are frequently referred to as the WGMs or morphology-dependent resonances (MDRs). A change in the shape, size, or refractive index of the micro-particle causes a shift in the WGM, which can be interpreted to obtain quantitative information about the stimulus causing the shift. The WGMs are characterized by very high optical quality factors, resulting in extremely narrow dips [13]. As a result, very small shifts in the WGMs caused by minute changes in the sensor morphology can be detected, for example, WGM shifts caused by forces as small as 10^{-5} N can be detected by using hollow polymethyl methacrylate (PMMA) sensors. Several WGM-based mechanical sensors have recently been proposed including temperature [14], concentration [15], pressure [16], acceleration [17], and force [18, 19]. The results of these studies are encouraging for the development of composites with embedded WGM-based sensors for structural health monitoring. It is possible to fabricate composite materials containing particles of glass or other optical materials that are of appropriate nature to provide functionalities of reinforcement and sensing at the same time.

It is also known that the use of hollow particles in WGM sensors provides significantly higher sensitivity compared to the solid particles of the same material [16, 19]. Such observation is a result of the lower effective elastic modulus of hollow particles compared to the solid particle of the same material, leading to higher deformation for the same applied force. Hence, syntactic foams, which are synthesized by dispersing hollow particles (microballoons) in polymers, have the potential to be developed as smart materials with high sensitivity. Figure 1, obtained from a published study [20], shows the microstructure of a syntactic foam reinforced with glass fibers. High volume fraction and random distribution of microballoons in syntactic foams result in the possibility that a micro-particle and a fiber would be suitably oriented to have the WGM sensing conditions satisfied. Figure 2a (adopted from [20]) shows remarkable similarities with Fig. 2b (adopted from [18]), which schematically shows the concept of WGM sensors created by optically coupling a dielectric microsphere with an optical fiber and exciting it by laser light. For that reason, development of smart syntactic foams based on WGM sensors seems like a realistic possibility. Development of such smart materials would integrate the microstructural and sensor design aspects. While experimental studies are required for realizing smart syntactic foams, theoretical modeling is needed in order to develop governing equations that can result in sensor calibration curves. The present study is focused on modeling and analyzing the sensitivity of such micro-optical sensor systems.

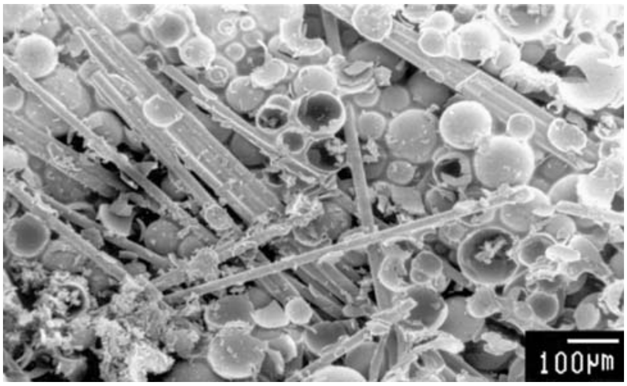

Fig. 1 Micrograph of a syntactic foam reinforced with glass fibers (adopted from [20])

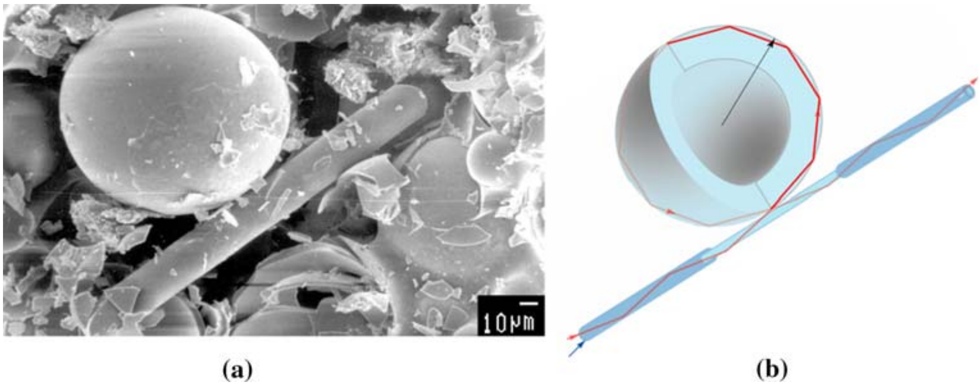

Fig. 2 **a** Interaction of a particle and a fiber in fiber-reinforced syntactic foams (adopted from [20]). **b** The concept of a whispering gallery mode sensor and its similarity to the fiber-reinforced syntactic foam microstructure

WGM sensors

A typical WGM sensor configuration is schematically shown in Fig. 3. Light from a tunable diode laser is coupled to a single mode optical fiber which serves as the input–output conduit. At the output end, the fiber is coupled to a photodetector that monitors the transmission spectrum through the fiber. When the evanescent fields of an exposed section of the fiber and the microsphere overlap, light coupling occurs between the fiber and the particle. If the refractive index of the surrounding medium is smaller than that of the particle, laser light coupled into the particle travels around the inner surface of the particle through multiples of total internal reflection. An optical resonance (WGM) will occur when the optical path length of the light traveling inside the particle is an integer multiple of the light wavelength. As the diode laser is tuned, WGMs are observed as sharp dips in the transmission spectrum through the fiber. Even a small change in the physical condition around the microsphere will perturb the morphology (shape, size, or refractive index) of the particle leading to a shift in the observed WGMs. Hence, if a mathematical relationship between the shift in WGMs and the change in the surrounding physical condition can be developed, the generic system shown in Fig. 3 can be configured as a sensor to measure a specific parameter such as stress or strain.

For the case when the radius of the microsphere is much larger than the wavelength of the interrogating laser ($R \gg \lambda$), the resonance condition can be approximated by

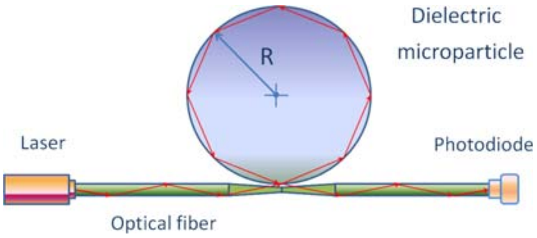

Fig. 3 Schematic of a whispering gallery mode sensor instrumentation

$$2\pi R n = l\lambda \tag{1}$$

where n and R are the refractive index and radius of the particle, respectively; λ is the vacuum wavelength of laser light; and l is an integer number. Therefore, any perturbation in the refractive index, Δn, or in the radius of the particle, ΔR, will cause a WGM shift of $\Delta\lambda$ as follows:

$$\frac{\Delta R}{R} + \frac{\Delta n}{n} = \frac{\Delta\lambda}{\lambda} \tag{2}$$

In the experimental studies, the value of $\Delta\lambda/\lambda$ is measured directly for the applied force. In the theoretical framework, the values of $\Delta R/R$ and $\Delta n/n$ need to be calculated for the applied force in order to obtain the total shift in WGMs.

Problem description

The embedded WGM sensor configuration assumed in this study is similar to the force sensor explored in [18] and [19]. As shown schematically in Fig. 4, the sensor measures compressive force applied along the polar direction (normal to the plane of light circulation in the sphere). The compressive force is relayed to the sphere through two platens as shown. Compression of the sphere along the

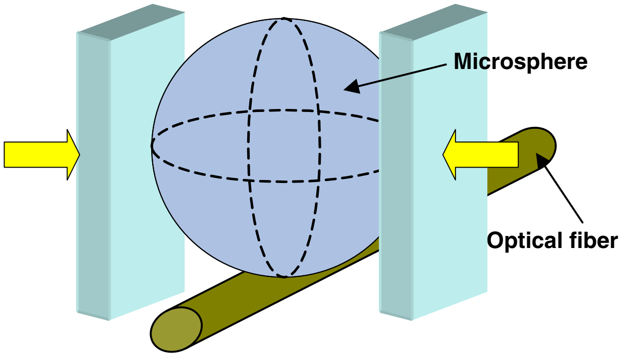

Fig. 4 Schematic representation of a WGM sensor setup to detect compressive force

polar direction will lead to a fractional change in both the index of refraction (due to stress) and the equatorial radius (strain) which will both induce a shift in the WGM as described in Eq. 2.

Quantitative information on the contribution of each of these effects on the total shift of WGM is required to interpret the information obtained from these sensors. The present work adopts a combination of analytical modeling and finite element analysis (FEA) to obtain quantitative values of each of these parameters for a given loading condition and develops theoretical calibration curves. The theoretical curves are validated with the experimental data of [19].

The sensor is modeled in two configurations, which are presented in Fig. 5. The first configuration has two solid platens compressing the particle (Fig. 5a) which represents the envisioned embedded stress sensor. However, in order to validate the present analysis against the published experimental results [19], the configuration used in that study (Fig. 5b) is also considered as the second case. In the second orientation [19], one of the platens is hollow for the ease of fixing the position of the microsphere on the plate. The analytical solution is derived for the first case and the FEA is conducted for both cases in the present study.

The platen–sphere configuration shown in Fig. 5 requires contact analysis. The contact problem was first proposed by Hertz [21]. Isotropic elastic spheres compressed by two rigid flat platens have been studied analytically by several researchers [22–26]. Some recent studies have worked on conducting FEA on such systems [27, 28]. The results obtained by Wu and Chau [26] have been adopted to develop the model framework for the WGM sensors.

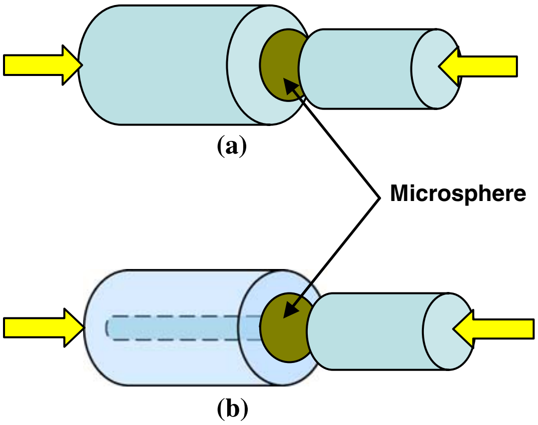

Fig. 5 Sphere compressed by **a** two solid platens and **b** a solid and a hollow platen

Analytical solutions

The Hertz contact theory is applied to model the sensor system because the uniform stress conditions will not represent well the contact stress between the surface of sphere and platens, especially at the center of the contact region [24]. In this theory the contact deformation of elastic bodies is considered in the absence of adhesion and friction. The theory has been experimentally shown to be valid at small deformations.

The Hertz contact conditions and various parameters used in the model are shown in Fig. 6. The boundary conditions for an isotropic sphere with radius R compressed between two rigid flat platens are in the same forms as those in uniform pressure load, but the applied load p is considered as a function of angle θ as [29]

$$\sigma_{rr} = \begin{cases} p(\theta) & 0 \le \theta \le \theta_0 \\ 0 & \theta_0 < \theta < \pi - \theta_0 \\ p(\theta) & \pi - \theta_0 \le \theta \le \pi \end{cases} \qquad (3)$$
$$\sigma_{r\theta} = \sigma_{r\phi} = 0 \text{ on } r = R$$

where the angle θ_0 is defined as the extent of the contact between the platen and the sphere, as shown in Fig. 6; r is the radial coordinate; and various σ are the stress components in the spherical coordinate system. The pressure p is calculated from the applied force F by using the relation

$$\begin{aligned} p(\theta) &= \frac{3F}{2\pi a_0^3}\sqrt{R^2\cos^2\theta - \left(R^2 - a_0^2\right)} \\ &= \frac{3F}{2\pi a_0^3}\sqrt{a_0^2 - R^2\sin^2\theta} \end{aligned} \qquad (4)$$

where a_0 is the radius of contact circle (Fig. 6). For the case of a deformable sphere in contact with rigid platens, a_0 is given by

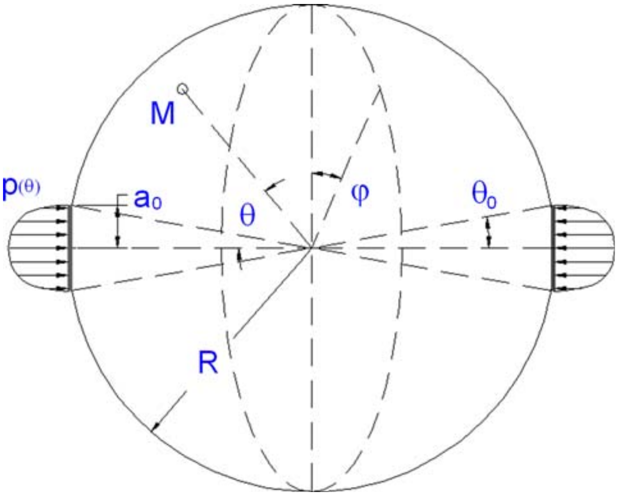

Fig. 6 The Hertz contact conditions for compression of a sphere by two platens

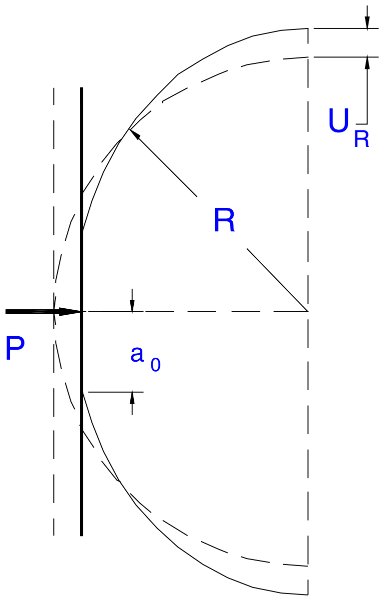

Fig. 7 Strain on the equator of the sphere under compression

$$a_0 = \left(\frac{3FR}{4E^*}\right)^{1/3} \tag{5}$$

where E^* is the contact modulus. For an elastic sphere in contact with rigid flat plates, contact modulus is the Young's modulus of the sphere [26].

The radial strain at a point on the surface of the sphere in the equatorial plane (in which the light travels) is of interest. Schematic representation of the problem is shown in Fig. 7. The radial strain, ε_R, is derived by dividing radial displacement U_r at $r = R$ by the initial radius of the sphere. U_r at any point in the sphere can be determined from the boundary conditions defined by [26]

$$\begin{aligned} U_r &= \sum_{m=0}^{\infty} U_{rm} \\ &= \sum_{m=0}^{\infty} \left[-\frac{m\bar{\lambda} + (m-1)\bar{\mu}}{(4m+3)\bar{\mu}} A_{2m} r^{2m+1} + 2mC_{2m} r^{2m-1} \right] \\ &\quad P_{2m}(\cos\,\theta) \end{aligned} \tag{6}$$

and, correspondingly, ε_R is calculated as

$$\varepsilon_R = \frac{U_R}{R} \tag{7}$$

where coefficients A_{2m} and C_{2m} depend on the applied loads. For Hertz contact, these coefficients are calculated from

$$\begin{cases} A_{2m} &= \frac{E_{2m}}{R^{2m}} \left[\frac{(4m+3)(2m+1)}{(8m^2+8m+3)\bar{\lambda} + 2(4m^2+2m+1)\bar{\mu}} \right] \\ A_{2m+1} &= 0 \\ C_{2m} &= \frac{4m(m+1)\bar{\lambda} + \left(4m^2+4m-1\right)\bar{\mu}}{2(2m-1)(2m+1)(4m+3)\bar{\mu}} R^{2m} A_{2m} \\ C_{2m+1} &= 0 \end{cases} \tag{8}$$

with

$$\begin{cases} E_{2m} = \frac{3(4m+1)F\sqrt{R^2-a_0^2}}{2\pi a_0^3} \int\limits_{\cos\theta_0}^{1} \left(\frac{x^2}{\cos^2\theta_0} - 1\right)^{1/2} P_{2m}(x)\mathrm{d}x \\ \cos\theta_0 = \frac{\sqrt{R^2-a_0^2}}{R},\ a_0 = \left[\frac{3FR(1-v^2)}{4E}\right]^{1/3},\ a_0 = R\sin\theta_0 \end{cases} \tag{9}$$

In these equations, P_{2m} (cos θ) is the Legendre polynomial of order $2m$, and $\bar{\lambda}$ and $\bar{\mu}$ are the Lame's constants which are related to Young's modulus E and Poisson's ratio v of the sphere through

$$\bar{\lambda} = \frac{Ev}{(1+v)(1-2v)}, \quad \bar{\mu} = \frac{E}{2(1+v)} \tag{10}$$

The Hertz boundary conditions are calculated analytically by summing up series terms of Eq. 6. The integral in E_{2m} is computed numerically, using Simpson's 1/3 rule [30]. However, the solution of the Hertz contact converged when $m \leq 20$, but it diverged when $m > 20$. The cause of the divergence was determined to be the integral in the equation of E_{2m} in (9). To evaluate the integral

$$I = \int\limits_{\cos\theta_0}^{1} \left(\frac{x^2}{\cos^2\,\theta_0} - 1\right)^{1/2} P_{2m}(x)\mathrm{d}x \tag{11}$$

numerically, the interval (cos θ_0, 1) is divided into 1,000 segments. For small deformations, cos $\theta_0 \approx 1$ (typically with $(1 - \cos\,\theta_0) \leq 10^{-4}$). In such a case, each interval is very small and truncation error can significantly affect the results. Hence, the exact value of x is calculated using Mathematica 5.1.

Finite element analysis

Model development

FEA is carried out on three-dimensional geometries shown in Fig. 5 using ANSYS 11.0. Symmetry allows for the analysis of only 1/16th of the actual geometry. Hence, the 360° cross section is reduced to a slice of 22.5° as shown in Fig. 8. This approach allows the use of a larger number of nodes in the analysis and reduces the computation time. The dimensions of each part are set the same as those in the actual WGM force measurement experiments [19]. The diameter and length of left platen are taken as 3.12 and 9.78 mm, respectively. The diameter and length of the right platen are taken as 1.47 and 4.52 mm, respectively. The diameter of hole in the case of hollow platen is taken as 150 μm (Fig. 5). The left platen is fixed at the left end

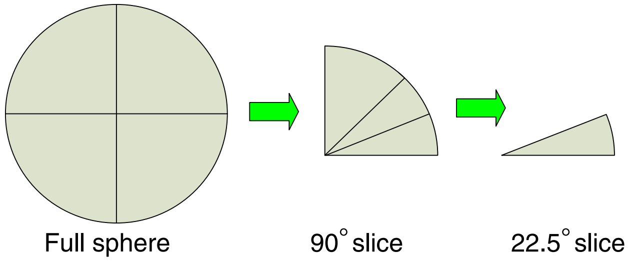

Fig. 8 Only 1/16th of the sphere is used in the FEA by applying appropriate symmetry conditions

and the load is applied on the right platen in all models. The diameter of the microsphere is varied from 100 to 800 μm in the FEA.

Elements used for the cylindrical platens and the sphere are *Solid186* and *Solid187*, respectively. The platens are discretized with larger size mesh because their deformation is not of interest in the present case. Meshing is controlled by defining the number of segment along the length and diameter of platens. The lines along the length of the platen are partitioned into larger segments than those along the cross section keeping the aspect ratio of each element within the allowable limits. The equatorial belt of the sphere that is of greatest interest has 20 predefined nodes along it for the convenience and accuracy of measuring the perimeter. The discretized model is shown in Fig. 9. The equatorial belt where strain is measured is marked in the figure. The contact between the sphere and the platens is modeled as flexible–flexible with the stiffness of the stiffer material assigned to each contact pair. Contact elements are 3D *targe170* and *conta175*. The solution is carried out by using Newton–Raphson method and the load is applied in 200 steps.

Steel 1018 and brass are used for the right and the left platen, respectively, in the compression test setup. Silica and PMMA microspheres are analyzed. Material properties used in the analyses are listed in Table 1.

FEA post-processing

As indicated by Eq. 2, both the radial strain ($\Delta R/R$) and the change in the index of refraction ($\Delta n/n$) need to be calculated in order to obtain the total WGM shift due to the applied force. $\Delta R/R$ is determined from the perimeter C of the equator shown in Fig. 9. The perimeter is computed in undeformed and deformed shapes of the microsphere by summing up the lengths of all the elements (Δl_i) along the equator. The difference between C_{deformed} and $C_{\text{undeformed}}$ is then divided by the undeformed circumference to get the circumferential strain ($\Delta C/C$); therefore, $\Delta R/R$ is obtained as follows:

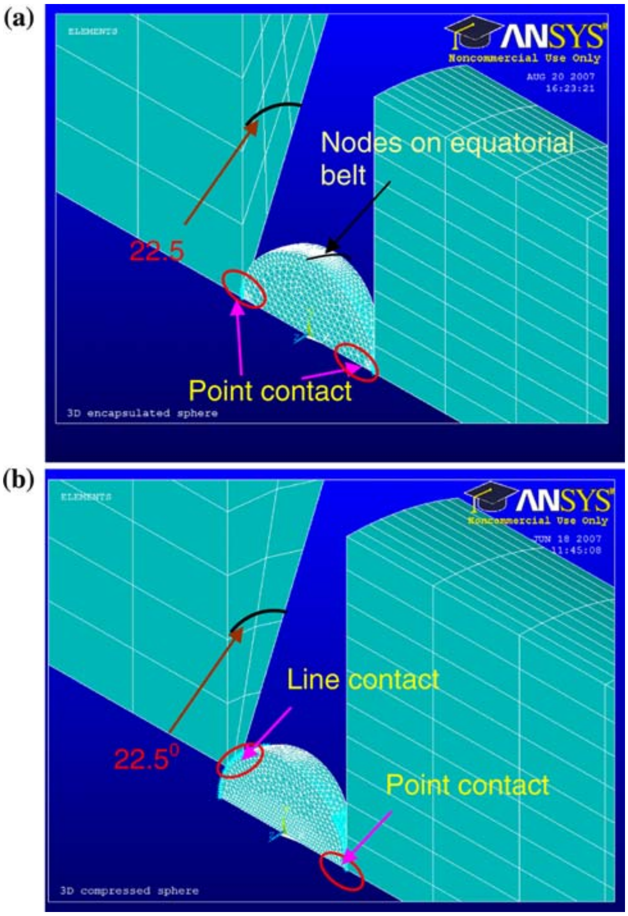

Fig. 9 Meshed finite element model and contact type in the compression of a particle using **a** solid–solid platens and **b** hollow–solid platens

Table 1 Material properties used in fem model (obtained from matweb.com)

Property	Steel 1018	Brass	Silica	PMMA
Young's modulus (GPa)	205	115	72.4	3.3
Poisson's ratio	0.29	0.31	0.19	0.35

$$\begin{aligned} C &= \sum_i \Delta l_i \\ \Delta C &= C_{\text{deformed}} - C_{\text{undeformed}} \\ \frac{\Delta R}{R} &= \frac{\Delta C}{C}, \quad (C = 2\pi R) \end{aligned} \tag{12}$$

$\Delta n/n$ is caused by a change in the local stress and is related to the elasto-optic properties of the material. The relationship between the refractive index and principal stresses is given by [31]

$$\begin{aligned} n_1 &= n_0 + C_1\sigma_1 + C_2(\sigma_2 + \sigma_3) \\ n_2 &= n_0 + C_1\sigma_2 + C_2(\sigma_1 + \sigma_3) \\ n_3 &= n_0 + C_1\sigma_3 + C_2(\sigma_1 + \sigma_2) \end{aligned} \tag{13}$$

Table 2 Elasto-optic coefficients and index of refraction (at room temperature)

Coefficient	Silica	PMMA
C_1 (m^2/N)	-4.2×10^{-12}	-10×10^{-12}
C_2 (m^2/N)	-0.65×10^{-12}	-10×10^{-12}
n_0	1.467	1.4876

where n_1, n_2, and n_3 are the local refractive indices in three principal directions corresponding to three principal stresses σ_1, σ_2, and σ_3, respectively. C_1 and C_2 are elasto-optic coefficients of the material and n_0 is the initial (stress free) index of refraction of the material, which are given in Table 2 [31–34]. The last two terms in Eq. 13 determine the stress-induced refractive index shift, Δn, in each principle direction. Note that the only relevant index shift is the one that is along the electric field direction of traveling light wave. Principal stresses can be directly obtained from the FEA solution but not the principal directions. However, principal directions at any point can be computed from six components of stress. Since points of interest are on the equatorial belt of the sphere, principal directions can be determined using principal stresses.

Once $\Delta R/R$ and $\Delta n/n$ are calculated separately, they can be combined to calculate the total WGM shift, $\Delta\lambda/\lambda$.

Model validation

As a first step, the meshed model is tested for accuracy by applying hydrostatic pressure on the sphere. The analytical solution for a sphere of volume V under hydrostatic pressure is given by

$$\frac{\Delta R}{R} = \frac{1}{3}\frac{\Delta V}{V} = \frac{p}{k} \tag{14}$$

where k is bulk modulus of the material, defined by

$$k = \frac{E}{3(1-2v)} \tag{15}$$

The $\Delta R/R$ obtained in the FEA, by measuring the length of each element along the equator before and after the deformation, is compared with the analytical solution. The results have shown that the error is less than 0.001% indicating that the FEA model is appropriate for the analysis.

Results and discussions

The total shift in WGMs can be calculated from Eq. 2, which requires estimation of strain and refractive index change due to the applied load. The calculations are repeated for a range of sphere sizes to obtain a theoretical "calibration curve" for each material that relates load sensitivity, $(\Delta\lambda/\lambda)/F$, to sphere diameter. The theoretical calibration curves are then compared to experimental results of [19], which are obtained using a setup similar to that shown in Fig. 5a and b using silica and PMMA microspheres. In these experiments, temperature is maintained constant because WGM sensors are sensitive to temperature changes also. The force ranges for the calibration of silica and PMMA sensors are 0–1 and 0–0.1 N, respectively.

A set of typical results for von-Mises stress, principle strain, and deformation profile obtained from FEA are shown in Fig. 10. Since the applied load is less than 1 N in the simulations, the visible effect of load is confined to a very small region near the sphere–platen contact. The numerical values of stress, strain, and displacement at the equator are used for the calculation of required parameters.

Calculation of strain

The values of radial strain per unit force in a microsphere compressed by two solid platens are obtained from the Hertz contact theory and FEA and are compared in Fig. 11. Results obtained from both methods show a very close match with each other over the entire sphere size range of 100–800 μm and for both silica and PMMA. The close matching between theoretical and FEA results further validates the model used in the study. The FEA results for a microsphere compressed between a solid and a hollow platen are also included in Fig. 11. It can be observed that for large D the strain values for both solid–solid and hollow–solid platens cases are essentially identical. However, for small D, the strain values start to diverge as D approaches the diameter of the hole in the hollow platen. Results show that the strain per unit force for PMMA is about 20 times higher than that of silica. Hence, the PMMA microsphere has a much higher sensitivity than the silica sensor.

Calculation of index of refraction change

The principal stresses on the equatorial plane of the optical path in the particle need to be determined in order to apply Eq. 13 for the calculation of $\Delta n/n$. The elasto-optic constants for silica and PMMA are taken from [31] and [33], respectively. The light is assumed to travel in a thin surface layer of the particle; hence, the principle stresses are determined only on the surface along the optical path. The equator of the sphere which is of current interest is shown in Fig. 9, and the notations for principal stresses on a surface element along that equator are shown in Fig. 12. The principal stresses in the direction of applied force and in the circumferential direction are compressive and tensile, respectively. The second principal stress component

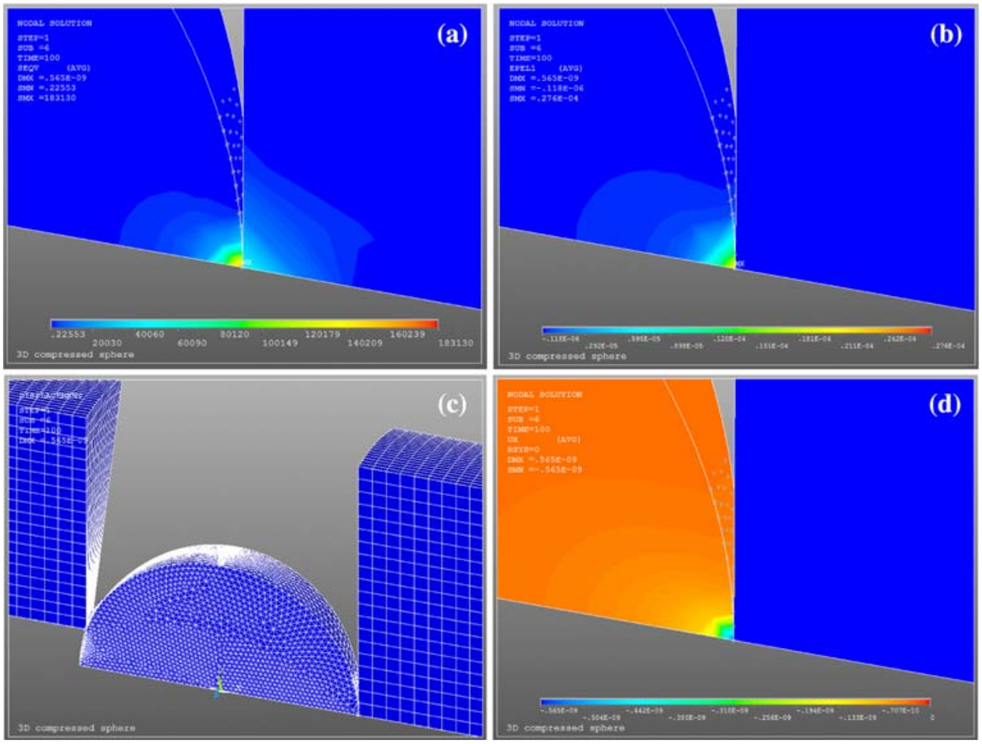

Fig. 10 **a** von-Mises stress. **b** Principal strain in applied force direction. **c** Deformation at the contact region. **d** Displacement in *x*-direction

(σ_2) is zero because of free boundary conditions. These stress values at various loads levels are determined from the FEA and substituted in Eq. 13 to calculate $\Delta n/n$.

Total WGM shift

The total WGM shifts are obtained by substituting the calculated values of $\Delta R/R$ and $\Delta n/n$ into Eq. 2. The experimental values of WGM shifts are taken from [19], which used laser wavelength of λ = 1,312 nm.

The experimental and calculated values of force-induced WGM shift slopes, $d\lambda/\lambda/F$, are plotted in Fig. 13a and b for silica and PMMA, respectively. The excellent agreement between the experiments and the computational results for PMMA shows that the theoretical model can accurately predict the $d\lambda/\lambda/F$ values for PMMA. For silica spheres, on the other hand, the FEA results provided higher estimates than the experimental values.

Several factors can lead to the discrepancy observed in the results for silica particles. One is related to the structure of the sphere material. PMMA does not have a crystal structure. Therefore, the speed of light propagating in the stressed material is not a function of the electric field direction, which implies that $C_1 = C_2$ in Eq. 13 [33]. Hence, transverse electric (TE) and transverse magnetic (TM) WGMs will experience the same index of refraction perturbation, Δn. Although silica is also generally amorphous, it can have some crystallinity in the structure based on the conditions of manufacturing the microspheres. Presence of any crystallinity, especially along the surface, will result in optical anisotropy inside the stressed microsphere. The wave propagation speed (i.e., refractive index) is a function of the electric field direction of the propagating wave, and n_1, n_2, and n_3 are not necessarily equal in the stressed silica sphere. Thus, unlike PMMA the amount of index perturbation, Δn, for silica depends on whether the observed WGM in the silica sphere is TE or TM mode. In Fig. 13, the values of $\Delta n/n$ are calculated assuming the experimentally observed WGMs are all TE modes. Figure 14 shows two separate curves: one calculated for TE mode and the other for TM mode for silica, along with the experimental results. For the TE mode, calculated refractive index shift along the applied load direction is used, whereas in the TM calculation, refractive index shift along the radial direction is used. It can be observed from the figure that the difference between TE and TM modes is small and the disagreement between the experimental data and the theoretical calculations is larger.

Another possible explanation for the observed discrepancy in the experimental and theoretical results could be that the microsphere and optical fiber are not aligned perfectly and the fiber axis is not parallel to the symmetric plane shown in Fig. 9a. In actual experiments the laser light may be coupled in a plane that makes a certain angle

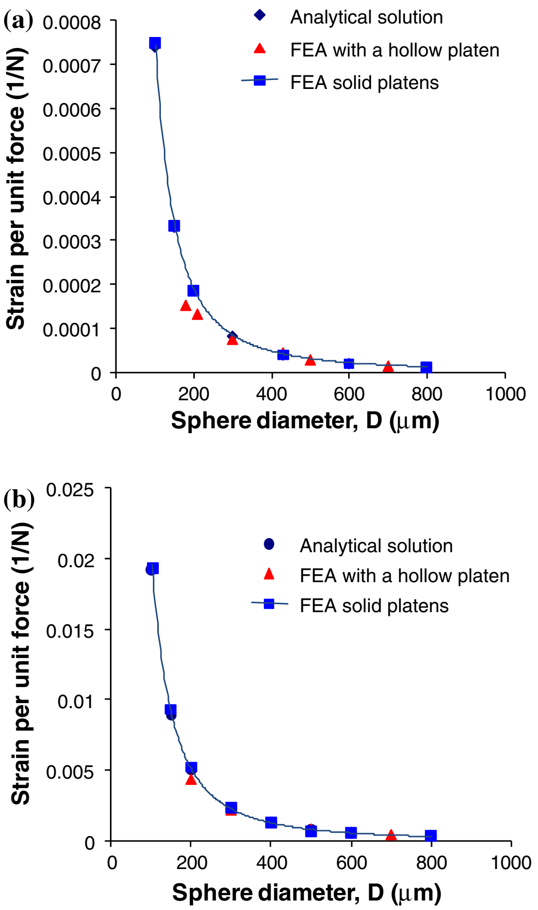

Fig. 11 Circumferential strain comparison between analytical solution and FEA for **a** silica and **b** PMMA microspheres

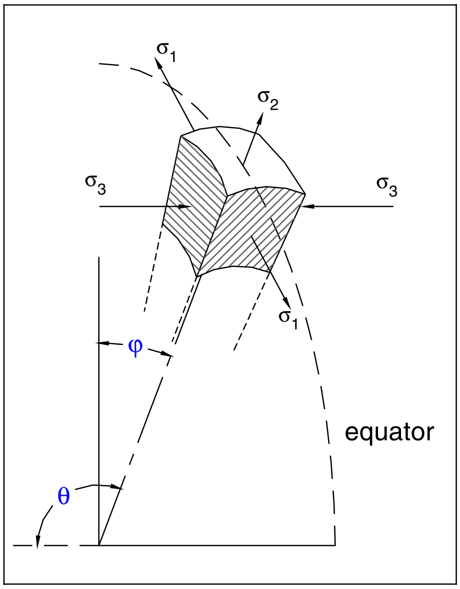

Fig. 12 Notations for stresses on a node on the equator where principal stresses are determined

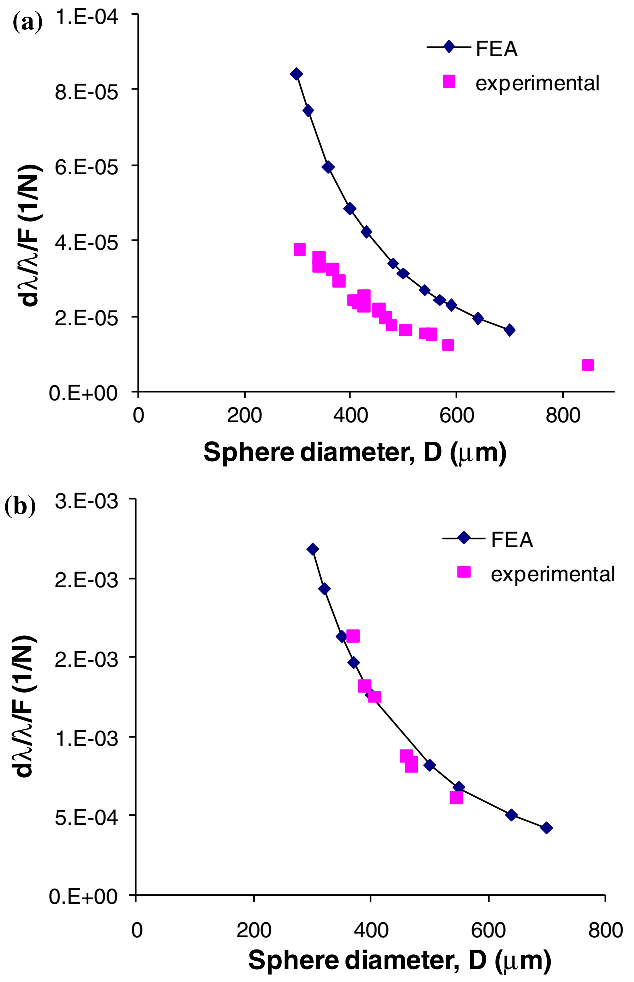

Fig. 13 Comparison of WGM shift in FEA and experiments for **a** silica and **b** PMMA

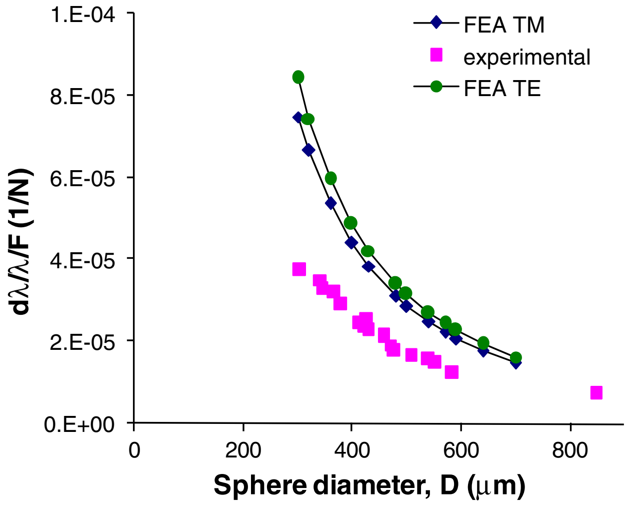

Fig. 14 Comparison of WGM shift for TE and TM modes of optical resonances and comparison with experimental data for a silica microsphere sensor

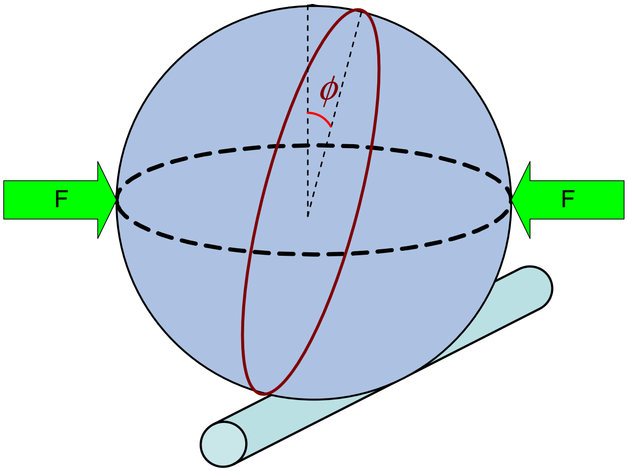

Fig. 15 Schematic showing light traveling in an orbit at angle ϕ to the symmetry plane

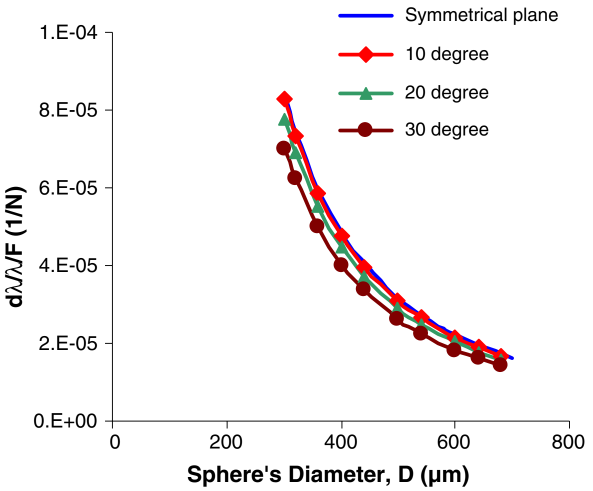

Fig. 16 Variation of WGM shift with coupling angle to the symmetry plane (10°, 20°, and 30°)

with respect to the assumed coupling direction (parallel to the platens) as shown in Fig. 15. In order to investigate the effect of such non-ideal coupling, the FEA is extended to inclined planes in the range of 0 to ±30° for ϕ to investigate the extent of coupling plane effects on WGM shifts. The results of this analysis are presented in Fig. 16. These results show that the strain and the index of refraction effects neutralize each other for planes that are within ±10° off-axis coupling and the calibration curve remains essentially the same. In the range of 10–30° off-axis coupling the calibration shifts slightly. Therefore, a possible imperfect light coupling into the spheres in the experimental work is not a likely reason for the discrepancy between experimental and numerical results. However, this result has important implications on the understanding of the WGM technique. The observation indicates that the precise coupling angle of light into the particle is not critical in the calibration of the sensors. Note that in the above calculations the effect of the curvature change on WGM shifts is assumed to be negligible.

The experimental results may be have been affected by several additional factors. The microspheres used in the experiments of [19] fabricated in our laboratory. The sphericity of such particles is not perfect and chemical composition can also vary within the structure of the microsphere. This can affect the experimental measurement of WGMs and also affect the sphere dimensions taken in the theoretical calculations. Also, the elasto-optic coefficients taken from the literature for silica may be in variance with the actual values for these experiments. Additionally, the degree of crystallinity in the particle is also expected to affect the results due to a change in the index of refraction. Considering the sensitivity of the WGM technique, small differences in these quantities can lead to the observed discrepancy in the calibration curves. However, the close matching of experimental and theoretical calibration curves for PMMA demonstrates the validity of the scheme adopted in the theoretical framework.

Development of smart composites

Solid and hollow particle filled composites have potential to be developed as smart materials with embedded WGM sensors. The size of the glass particles used in composites materials, 20–500 μm, coincides with that used in WGM sensors. The smart syntactic foams can be especially useful in aerospace and marine applications due to their low density, high specific strength, and high damage tolerance, if the structural health-monitoring capabilities are integrated in the material [35, 36].

Several challenges remain in developing such embedded sensor systems. The mismatch between the thermal expansion coefficients of the fiber and the polymeric resin can lead to the fracture of the fiber. Additionally, to obtain high optical Q-factors for the resonances (allowing for high sensitivities), the optical losses in the sensor system should be minimized. One type of loss, which tends to be significant, is due to impurities in the particle material leading to significant light absorption. Another type of loss is scattering through the particle-encapsulating resin interface. To minimize scattering losses, the interface has to be a highly smooth surface and the refractive index difference between the particle and the encapsulating resin has to be sufficiently large. In addition, the resin used as the matrix material should have lower index of refraction compared to the materials of microsphere and optical fiber.

The theoretical framework developed in the present study needs to be extended to sensor systems encapsulated in polymeric resins, which will represent the actual structure of syntactic foams. However, some challenges still remain. For example, as present results indicate, the calibration curve for PMMA sensors could be developed based on theoretical analysis but a similar curve for silica sensors may have an offset compared to the experimental values which, at present, is unexplained. Additional factors that affect the behavior of silica sensors need to be characterized and incorporated in the model. The result that slight variations in the coupling angle between the particle and the fiber will result in the same calibration curve indicates that such smart materials may eventually be developed by using bulk processing methods available for syntactic foams.

Conclusions

The technique to measure strain using WGM sensors is analyzed by developing a theoretical framework. A combination of analytical and FEA methods is used to calculate the strain and change in the index of refraction of the microsphere material, which are combined to obtain the shift in WGM. The results show that the analytical framework can accurately predict the behavior of PMMA microspheres. In case of silica microspheres, there is some quantitative discrepancy. Several parameters are identified to account for the differences, which need further study. These parameters include the possibility of having some crystallinity in the silica sphere, coupling of light in a plane that is not the primary equatorial plane, and measurement uncertainties. The development of theoretical framework is an essential step in developing smart materials containing WGM sensors. Particulate composites provide the best opportunities to integrate WGM sensors in their structure. The possibility of using these sensors in syntactic foams is also explored where hollow particles can act as sensors. The theoretical model developed in this work will be extended to the sensor system embedded in a polymeric resin in our further work.

Acknowledgement This research work is supported by the National Science Foundation grant #CBET-0619193.

References

1. Morey WW (1990) Distributed fiber grating sensors. In: Proceedings of international conference on optical fiber sensors, Sydney, pp 285–288
2. Melle SM, Liu K, Measures R (1991) Strain sensing using a fiber optical Bragg grating. In: Claus RO, Udd E (eds) Proceedings of fiber optic smart structures and skins IV, SPIE, vol 1588, Boston, MA, 5 Sept 1991
3. Foote PD (1994) Fiber Bragg grating strain sensors for aerospace smart structures. In: McDonach A, Gardiner PT, McEwen RS, Culshaw B (eds) Proceedings of 2nd European conference on smart structures and materials, SPIE, vol 2361, Glasgow, UK, 12 Oct 1995
4. Kim KS, Ismailm Y, Springer GS (1993) J Compos Mater 27:1663
5. Habel WR, Hofmann D (1994) Strain measurements in reinforced concrete wall during the hydration reaction by means of embedded fiber interferometers. In: McDonach A, Gardiner PT, McEwen RS, Culshaw B (eds) Proceedings of 2nd European conference on smart structures and materials, SPIE, vol 2361, Glasgow, UK, 12 Oct 1995
6. Rashleigh SC (1983) Polarimetric sensors: exploiting the axial stress in high birefringence fibers. In: Proceedings of 1st international conference on optical fiber sensors, IEE, London, pp 210–213
7. Jackson DA (1985) J Phys E18:981
8. Inandi D, Elamar A, Vurpillot S (1994) Low coherence interferometry for the monitoring of civil engineering structures. In: McDonach A, Gardiner PT, McEwen RS, Culshaw B (eds) Proceedings of 2nd European conference on smart structures and materials, SPIE, vol 2361, Glasgow, UK, 12 Oct 1995
9. Maharsia R, Gupta N, Jerro HD, Peck JA (2003) Evaluation of change in mechanical properties due to the incorporation of optical fiber sensors in glass fiber reinforced composite pipes. In: Proceedings of American society for composites 18th annual conference, Paper #125, Gainesville, 19–22 Oct 2003
10. de Olivera R, Ramos CA, Marques AT (2007) Compu Struct. doi: 10.1016/j.compstruc.2007.01.040
11. Liu G, Chuang SL (1998) Sens Actuators A 69:143
12. Wang Q, Grattan KTV, Palmer AW (1998) Sens Actuators A 71:179
13. Matsko AB, Savchenkov AA, Strekalov D et al (2005) Review of application of whispering-gallery mode resonators in photonics and nonlinear optics. IPN progress report 42-162. http://tmo.jpl.nasa.gov/progress_report/42-162/162D.pdf
14. Guan G, Arnold S, Ötügen VM (2006) AIAA 44:2385
15. Das N, Ioppolo T, Ötügen V (2007) Investigation of a micro-optical concentration sensor concept based on whispering gallery mode resonators. Presented at the 45th AIAA aerospace sciences meeting and exhibition, Reno, 8–11 Jan 2007
16. Ioppolo T, Ötügen V (2007) J Opt Soc Am B 24:2721–2726
17. Laine JP, Tapalian C, Little B, Haus H (2001) Sens Actuators A 93:1
18. Kozhevnikov M, Ioppolo T, Stepaniuk V et al (2006) Optical force sensor based on whispering gallery modes resonators. AIAA-2006-649, Reno, 9–12 Jan 2006
19. Ioppolo T, Kozhevnikov M, Stepaniuk V, Ötügen VM, Sheverev V (2008) Appl Opt 47:3009
20. Gupta N, Woldesenbet E, Kishore (2002) J Mater Sci 37:3199. doi:10.1023/A:1016166529841
21. Briscoe BJ, Liu KK, Williams DR (1997) J Colloid Interface Sci 200:256
22. Sternberg E, Rosenthal F (1952) J Appl Mech 19:413
23. Hiramatsu Y, Oka Y (1966) Int J Rock Mech Min Sci 3:89
24. Chau KT, Wei XX, Wong RHC et al (2000) Mech Mater 32:543
25. Chau KT, Wei XX (1999) Int J Solids Struct 36:4437
26. Wu SZ, Chau KT (2006) Mech Mater 38:1039
27. Kienzler R, Schmitt W (1990) Powder Technol 61:29
28. Carlisle KB, Lewis M, Chawla KK et al (2007) Acta Mater 55:2301
29. Timoshenko SP, Goodier JN (1973) Theory of elasticity, 3rd edn. McGraw-Hill, New York
30. Chapra SC, Canale RP (2005) Numerical methods for engineers, 5th edn. McGraw-Hill, New York

31. Belluard Y, Columb T, Depeursinge C et al (2006) Opt Express 14:8360
32. Rudd JF, Gurnee EF (1957) J Appl Phys 28:1096
33. Ay F, Kocabas A, Kocabas C et al (2004) J Appl Phys 96:7147
34. Primak W, Post D (1959) J Appl Phys 30:779
35. Gupta N, Kishore, Woldesenbet E et al (2001) J Mater Sci 36:4485. doi:10.1023/A:1017986820603
36. Gupta N, Woldesenbet E, Mensah P (2004) Compos Part A 35:103